Error Structure and Atmospheric Temperature Trends in Observations from the Microwave Sounding Unit

CHENG-ZHI ZOU

Center for Satellite Applications and Research, NOAA/NESDIS, Camp Springs, Maryland

MEI GAO

Center for Satellite Applications and Research, NOAA/NESDIS, Camp Springs, Maryland, and Chinese Academy of Meteorological Sciences, China Meteorological Administration, Beijing, China

MITCHELL D. GOLDBERG

Center for Satellite Applications and Research, NOAA/NESDIS, Camp Springs, Maryland

ABSTRACT

The Microwave Sounding Unit (MSU) onboard the National Oceanic and Atmospheric Administration polar-orbiting satellites measures the atmospheric temperature from the surface to the lower stratosphere under all weather conditions, excluding precipitation. Although designed primarily for monitoring weather processes, the MSU observations have been extensively used for detecting climate trends, and calibration errors are a major source of uncertainty. To reduce this uncertainty, an intercalibration method based on the simultaneous nadir overpass (SNO) matchups for the MSU instruments on satellites *NOAA-10*, *-11*, *-12*, and *-14* was developed. Due to orbital geometry, the SNO matchups are confined to the polar regions, where the brightness temperature range is slightly smaller than the global range. Nevertheless, the resulting calibration coefficients are applied globally to the entire life cycle of an MSU satellite.

Such intercalibration reduces intersatellite biases by an order of magnitude compared to prelaunch calibration and, thus, results in well-merged time series for the MSU channels 2, 3, and 4, which respectively represent the deep layer temperature of the midtroposphere (T_2), tropopause (T_3), and lower stratosphere (T_4). Focusing on the global atmosphere over ocean surfaces, trends for the SNO-calibrated T_2, T_3, and T_4 are, respectively, 0.21 ± 0.07, 0.08 ± 0.08, and -0.38 ± 0.27 K decade^{-1} from 1987 to 2006. These trends are independent of the number of limb-corrected footprints used in the dataset, and trend differences are marginal for varying bias correction techniques for merging the overlapping satellites on top of the SNO calibration.

The spatial pattern of the trends reveals the tropical midtroposphere to have warmed at a rate of 0.28 ± 0.19 K decade^{-1}, while the Arctic atmosphere warmed 2 to 3 times faster than the global average. The troposphere and lower stratosphere, however, cooled across the southern Indian and Atlantic Oceans adjacent to the Antarctic continent. To remove the stratospheric cooling effect in T_2, channel trends from T_2 and T_3 (T_{23}) and T_2 and T_4 (T_{24}) were combined. The trend patterns for T_{23} and T_{24} are in close agreement, suggesting internal consistencies for the trend patterns of the three channels.

1. Introduction

Accurate determinations of global and regional temperature trends are crucial for framing policy decisions

Corresponding author address: Dr. Cheng-Zhi Zou, Room 712, 5200 Auth Road, Center for Satellite Applications and Research, NOAA/NESDIS, NOAA Science Center, Camp Springs, MD 20746.
E-mail: cheng-zhi.zou@noaa.gov

on prevention, mitigation, and adaptation strategies for global warming. Several different observational analyses indicate that the earth's surface has warmed at a rate of 0.17 K decade^{-1} during the last 30 years (Solomon et al. 2007). Confidence in the surface temperature trend is high owing to the relatively dense surface observational network. However, determining the temperature trend of the earth's atmosphere and its spatial structure remains a challenge. Temperature trends derived from conventional radiosonde observations are

questionable because they are subject to large regional and temporal errors due to varying observational practices in different countries. In addition, radiosonde stations are too sparse for determining spatial trend patterns. The Microwave Sounding Unit (MSU) on board the NOAA polar-orbiting satellites is uniquely positioned to provide the global coverage needed for measuring atmospheric temperature trends. However, temperature trends obtained from these observations are still under debate; different results are obtained by different investigators. Further investigation is required to reconcile these differences.

R. W. Spencer and J. R. Christy pioneered the use of MSU observations for climate trend detection. MSU observations contain 11 pixels per scan line with the central pixel being the nadir view of the earth. The ground resolution of the nadir view is 110 km. In their initial studies, Spencer and Christy (1992a,b) constructed two temperature products from the MSU channel-2 (53.74 GHz) observations—T_2 and temperature lower troposphere (TLT)—using different combinations of viewing angles. An average of the MSU channel-2 data over seven near-nadir views, T_2 represented the mean midtropospheric temperature from the surface to about 15 km. TLT was a weighted difference between four near-limb and four near-nadir views, and its weighting function peaked in the lower troposphere. The trends for T_2 and TLT were found to be only 0.02 and 0.04 K decade^{-1}, respectively, for the 1979–90 period (Spencer and Christy 1992a,b).

The initial Spencer and Christy (1992a) study was followed by a series of investigations addressing different issues in the MSU data processing and trend determination. These problems include orbital decay (Wentz and Schabel 1998), diurnal cycle drift effect (Trenberth and Hurrell 1997; Christy et al. 1998, 2000; Fu and Johanson 2005; Mears and Wentz 2005; Randall and Herman 2008), orbital drift-related warm target contamination (Christy et al. 2000; Mears et al. 2003; Zou et al. 2006), nonlinear calibration (Grody et al. 2004; Zou et al. 2006), short overlap between *NOAA-9* and *NOAA-10* (Mears and Wentz 2005), intersatellite bias removal and merging procedure (Christy et al. 1998, 2000, 2003; Hurrell and Trenberth 1998; Prabhakara and Iacovazzi 1999; Prabhakara et al. 2000; Mears et al. 2003; Vinnikov and Grody 2003; Grody et al. 2004; Vinnikov et al. 2006; Zou et al. 2006), stratospheric effect on T_2 (Spencer and Christy 1992b; Fu et al. 2004; Fu and Johanson 2004, 2005; Spencer et al. 2006; Johanson and Fu 2006), and noise in the TLT product (Hurrell and Trenberth 1997, 1998).

Among the aforementioned problems, the warm target contamination and intersatellite bias are related to calibration errors. Empirical correction techniques have been developed by Christy et al. (2000, 2003), Mears et al. (2003), and Grody et al. (2004) to remove intersatellite biases for satellite merging. Prior to the empirical corrections, however, diurnal cycle correction should be applied. Therefore, errors in the diurnal correction were brought into the merging procedure, which may amplify trend uncertainties (Mears and Wentz 2005). To reconcile the problem, Zou et al. (2006) have developed an intercalibration procedure to merge the MSU satellites using simultaneous nadir overpasses (SNO). Unlike previous corrections, SNO intercalibration removes intersatellite biases and warm target contamination at the radiance level by providing a more accurate determination of the sensor nonlinearity. This method removes intersatellite biases before a diurnal drift correction is applied; therefore, it is not closely tied to the diurnal correction algorithm.

Despite the enhanced understanding of MSU data processing, differences in trend results still exist among different research groups. Furthermore, the spatial trend pattern from the MSU observations has not been fully investigated because of spatial dependency of the intersatellite biases. This study provides a comprehensive assessment of the SNO calibration results and their comparisons with other empirical correction techniques. These results include the calibration coefficients, intersatellite bias statistics, and long-term MSU trends. Both global ocean means and spatial patterns of trends are investigated in this study. We show that the SNO-calibrated temperature trends are relatively stable when different samplings and merging techniques are applied in the time series. In our previous study (Zou et al. 2006), only the calibration results for MSU channel 2 were described. This study extends these works to MSU channels 3 and 4 (54.96 and 57.95 GHz, respectively, hereafter T_3 and T_4).

To focus on the calibration and merging procedure and to limit trend uncertainty, we constrain our study only to the data and products for which certain effects are small. In particular, we use observations from *NOAA-10* and after (1987 to the present) and focus on T_2, T_3, and T_4 products so that the effects of orbital decay and short overlap between *NOAA-9* and *-10* are ignored. Also, only trend patterns over the ocean area are provided for T_2, so the diurnal drift effect can be ignored (Mears et al. 2003; Vinnikov and Grody 2003).

The rest of this study describes the SNO nonlinear calibration method (section 2), the global trend results for MSU channels 2, 3, and 4 (section 3), the spatial pattern of the intersatellite biases and trends (section 4), and, finally, our conclusions (section 5).

2. The SNO calibration methodology

The SNO calibration procedure deals directly with the raw count data of MSU observations. Essentially, MSU uses an on-orbit calibration method that includes two calibration targets: the cosmic cold space and an onboard blackbody warm target. The cold space has a temperature of 2.73 K, and the warm target temperature is measured by the platinum resistance thermometers embedded in the blackbody target. In each scan cycle, the MSU looks at these targets as well as the earth, and the signals from these "looks" are processed by the instrument and recorded as electric voltage in the format of digital counts. The root-level (level 1c) calibration converts the digital count of the earth scene look to the earth scene radiance using the two calibration targets as the end-point references. The calibration equation is written as (Zou et al. 2006)

$$R = R_L - \delta R + \mu Z, \tag{1}$$

where R is the earth radiance, $R_L = R_c + S(C_e - C_c)$, representing the dominant linear response, and $Z = S^2(C_e - C_c)(C_e - C_w)$ is a nonlinear response. Here C represents the raw counts (electric voltage output) and

$$S = \frac{R_w - R_c}{C_w - C_c}$$

is the slope determined by the two calibration points. The subscripts e, w, and c refer to the earth-view scene, onboard warm blackbody target, and cold space, respectively; δR represents a radiance offset; and μ is a nonlinear coefficient. The cold space radiance R_c is specified to be 9.6×10^{-5} mW (sr m^2 cm^{-1})$^{-1}$ for all scan lines. This corresponds to a brightness temperature of 4.78 K that includes the cold-space temperature of 2.73 K plus an increase of about 2 K owing to the antenna sidelobe radiation. The nonlinear coefficient μ is a function of the MSU instrument body temperature (Mo et al. 2001), but is assumed to be a constant in this study since its variation range is small (Zou et al. 2006). The algorithm to compute R_w can be found in the NOAA Polar Orbiter data user's guide (Kidwell 1998). Once the radiance is known, the brightness temperature T_b is computed using the Planck function.

Equation (1) is a modified version of the calibration algorithm originally suggested by Mo (1995), where δR was assumed to be zero and the nonlinear coefficient μ was obtained from prelaunch chamber test datasets (Mo et al. 2001). This prelaunch calibration was conducted for each MSU independently. Because of the independency and orbital changes after launch, the prelaunch calibration left residual time-changing biases $O(0.5$ K) between satellites. To remove intersatellite biases, the offset δR is included in Eq. (1), so the algorithm is allowed for intercalibration using the SNO matchups (Zou et al. 2006). The SNO matchups contain simultaneous observations that are less than 2 min apart and within 111 km ground distance apart for the nadir pixels from any NOAA satellite pairs. The SNO sampling numbers were found to increase exponentially with increases of the SNO separation distance between the two satellites. The 111-km separation was selected to balance the two requirements for the SNO matchups: the SNO separation distance should be as small as possible, but there should be sufficient samplings within that distance for good statistics (Zou et al. 2006). The SNO generation, error characteristics, and their advantages for satellite intercalibration are described in details in Cao et al. (2004) and Zou et al. (2006).

Using the SNO matchups, Zou et al. (2006) developed a sequential procedure to obtain the calibration coefficients, δR and μ, for MSU channel 2 on board *NOAA-10*, *-11*, *-12*, and *-14*. This sequential procedure is summarized in the appendix and is used here again to obtain calibration coefficients for MSU channels 3 and 4 for these same satellites. The results are listed in Table 1. The coefficients for channel 2 obtained by Zou et al. (2006) are also listed for completeness. The nonlinear coefficients obtained from the postlaunch SNO sequential procedure are all in the same sign as obtained from the prelaunch calibration using chamber test datasets (Mo et al. 2001), but values of the former method are one to two times larger than the later one for *NOAA-12* and *NOAA-14*. These larger nonlinear coefficients result from the requirement of bias drift removal in the radiance calibration owing to orbital-drift related warm target contamination (see the appendix).

Due to geometry of the NOAA polar-orbiting satellites, the SNO matchups are available only over the polar regions (70°–80° north or south), where the brightness temperature range is slightly smaller than it is globally. Nevertheless, the calibration coefficients obtained from these matchups are applied globally for the entire life cycle of an MSU satellite. Using the obtained calibration coefficients, a global level-1c radiance dataset is generated from Eq. (1). Next, a limb correction is applied to these radiances to correct different incident angles of the off-nadir footprints to the nadir direction. This correction is necessary so that the off-nadir footprints can be used in the time series to increase observation samplings and reduce noise and sampling-related biases. The scheme suggested by Smith et al. (1974), which uses all available channels in a linear combination, is used for the limb adjustment. The limb correction coefficients are obtained using a statistical method developed by Goldberg et al. (2001) based on global *NOAA-10* observations during January 1987.

TABLE 1. Calibration coefficients for MSU channels (Ch 2, 3, and 4) for different satellites obtained from the SNO sequential procedure. Units for δR and μ are in 10^{-5} (mW) (sr m^2 cm^{-1})$^{-1}$ and (sr m^2 cm^{-1}) (mW)$^{-1}$, respectively. The channel 2 coefficients were obtained in Zou et al. (2006) and are listed here again for completeness.

Satellite NOAA-	δR (channel Ch2)	μ (Ch 2)	δR (Ch3)	μ (Ch 3)	δR (Ch 4)	μ (Ch 4)
10	0	6.25	0	5.63	0	4.95
11	−2.4641	9.5909	−1.9983	7.1892	−0.7271	5.4574
12	−0.0996	6.7706	−2.3979	8.3282	−4.6074	7.1040
14	−0.6363	7.4695	−3.0810	8.7525	−0.7753	5.4175

After the limb correction, the corrected radiances are binned together to generate a pentad T_b dataset with grid resolution of 2.5° latitude by 2.5° longitude. A total of seven near-nadir footprints per scan line are first used in our time series analysis in the following section, but the effect of the limb correction on the error characteristics and trend pattern will be investigated in detail in section 4. It will be shown that, although the limb correction coefficients are obtained from observations of a specific time period, they work for all the MSU observations because increasing the total number of limb-corrected footprints reduces the intersatellite biases while the trend remains the same.

3. Global ocean mean trends

We computed the global ocean means from the gridded T_b dataset and use $\langle \Delta T_{j,k} \rangle$ to represent the ocean mean temperature difference between satellites j and k. Figures 1a–c examine the error characteristics (bias and standard deviation) of the SNO intercalibration by providing a comprehensive comparison of the $\langle \Delta T_{j,k} \rangle$ time series between different calibration and correction procedures for MSU channels 2, 3, and 4, respectively. For each panel, the bottom three traces show $\langle \Delta T_{j,k} \rangle$ for three different calibration approaches, while the upper three traces show $\langle \Delta T_{j,k} \rangle$ after three different corrections on top of the SNO calibration.

As a benchmark in characterizing the MSU error structure, we first show the $\langle \Delta T_{j,k} \rangle$ time series for the linear calibration (the bottom trace) where only the linear part in Eq. (1), R_L, is used in the level-1c calibration. Then the $\langle \Delta T_{j,k} \rangle$ time series for the NOAA operational calibration (the second trace from the bottom) and the SNO calibration (the third trace from the bottom) are shown for a comparison. Note that the limb correction and binning procedures are all the same for these three different calibrations. As shown, the linear calibration and NOAA operational calibration result in intersatellite biases that are a few tenths of a degree (Kelvin), and these biases change with time owing to orbital drift-related warm target contamination. The average standard deviation (σ hereafter) over the dif-

ferent overlaps for the linear calibration is 0.186, 0.191, and 0.167 K for channels 2, 3, and 4, respectively. These numbers are reduced by half in the NOAA operational calibration.

After the SNO calibration, this warm target contamination is mostly removed for channels 2 and 4, but small fluctuations for channel 3 for the NOAA-12–NOAA-11 time series still exist. Despite the problems in NOAA-12–NOAA-11 of channel 3, the overall fluctuations for the SNO calibrations are much smaller than the linear and NOAA operational calibrations, reflected by the small averages of σ (0.035, 0.046, and 0.050 K for channels 2, 3, and 4, respectively). This occurs because the final calibration coefficients are chosen to minimize the overall warm target contamination in all satellites (see the appendix for more details).

After the SNO calibration, the intersatellite biases become nearly a constant (i.e., no drift) and are an order of magnitude smaller than the linear and NOAA operational calibrations. Although small, these biases must be completely removed to construct merged time series. We use different methods to remove these biases to obtain the merged time series and trends. The first approach is to simply remove constant intersatellite biases to get a corrected global ocean mean time series, still using NOAA-10 as a reference. As shown in Fig. 1, this approach (the fourth trace from the bottom) removes intersatellite biases, but the small fluctuations in $\langle \Delta T_{N11,N12} \rangle$ of channel 3 in the SNO calibration remain.

In the second and third correction approaches, we apply methods developed by Christy et al. (2000), Mears et al. (2003), and Grody et al. (2004), in which the $\langle \Delta T_{j,k} \rangle$ is assumed to be empirically related to the warm target temperature of the overpass satellites. In the Christy et al. (2000, 2003) and Mears et al. (2003) approach (hereafter the Christy correction), the relationship is linear,

$$\langle \Delta T_{j,k} \rangle = \text{bias}_{j,k} + a_j T'_w(j) + a_k T'_w(k), \qquad (2)$$

where T'_w is the $\langle T_w \rangle$ anomaly with $\langle T_w \rangle$ being the global ocean mean warm target temperature. However, in the
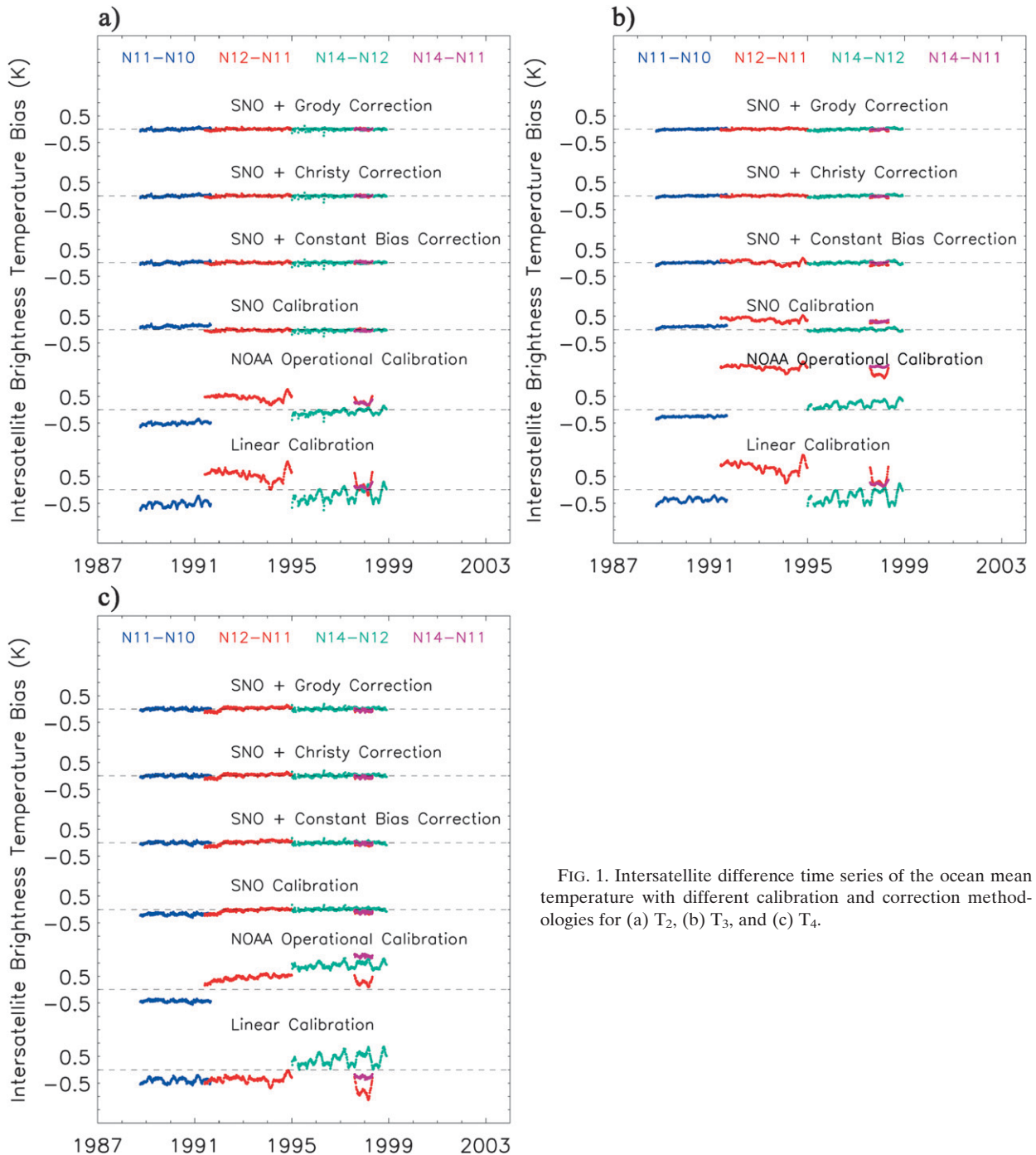
FIG. 1. Intersatellite difference time series of the ocean mean temperature with different calibration and correction methodologies for (a) T_2, (b) T_3, and (c) T_4.

Grody et al. (2004) correction (hereafter the Grody correction), the relationship is expressed as

$$\langle \Delta T_{j,k} \rangle = \text{bias}_{j,k} + a'_j G(j) + a'_k G(k), \qquad (3)$$

where $G = (\langle T_b \rangle - T_c)(\langle T_w \rangle - \langle T_b \rangle)$; here, $\langle T_b \rangle$ is the global ocean-averaged brightness temperature after the SNO calibration, and T_c (= 4.78 K) is a cold space

temperature plus a sidelobe effect. The quantity G is also linearly related to the warm target temperature anomaly, but the anomaly is relative to a varying brightness temperature and the target factor $[a'(\langle T_b \rangle - T_c)]$ is also changing with the brightness temperature. In the globally averaged situation, the variation of T_b is much smaller than T_w, meaning the global mean G behaves

TABLE 2. Temperature anomaly trends of the ocean mean MSU time series for the time period from January 1987 to September 2006 for different channels. Errors are computed for a 95% confidence interval with autocorrelation adjustment. Units are in K decade^{-1}.

	SNO + constant bias correction	SNO + Christy correction	SNO + Grody correction	Percent difference between maximum and minimum trend	Averages over different methods
T_2	0.234 ± 0.071	0.197 ± 0.068	0.204 ± 0.069	17	0.212 ± 0.069
T_3	0.079 ± 0.085	0.060 ± 0.082	0.067 ± 0.082	27	0.069 ± 0.083
T_4	-0.414 ± 0.287	-0.336 ± 0.271	-0.340 ± 0.272	21	-0.363 ± 0.276

similarly to the global mean T_w. Therefore, as we discuss shortly, the two correction approaches provide similar results on the ocean mean trends. However, the results on trend patterns are very different.

For the four overlaps shown in Fig. 1, we constructed a series of seven regression equations and solve for the coefficients in the empirical equations (2) or (3) by minimizing the differences between the two sides of the equations. Then we obtained the corrected T_b time series for different satellites by subtracting the empirical corrections using *NOAA-10* as a reference. The top two traces in Fig. 1 show the $\langle \Delta T_{j,k} \rangle$ time series after these corrections. The averaged σ after these corrections is nearly equal to the SNO calibration for channels 2 and 4 but ~0.015 K smaller than the SNO calibration for channel 3. This smaller σ results from further reduction of fluctuations in the *NOAA-12–NOAA-11* time series. This result is expected since more coefficients are introduced to remove the warm target temperature contamination. However, for channels 2 and 4, where the SNO calibration has already successfully removed the T_w contamination, the Christy and Grody corrections do not improve the σ. In all of these corrections, both the intersatellite biases and the trends of the different time series are nearly reduced to zero, so they do not affect the trends of the merged time series. However, even after the different adjustments are applied, there is still a bias for the first few months of *NOAA-12–NOAA-11* of channel 4 that appears to be unrelated to T_w. The reason for this bias is unclear.

After the intersatellite biases were removed, a single time series was constructed by averaging all observations from different satellites, and temperature anomaly trends were then computed for the merged time series. Here the anomaly time series was obtained by subtracting the mean annual cycle of the merged time series. The anomaly trends of T_2, T_3, and T_4 from 1987 to 2007 and their associated 95% confidence intervals for the three different calibration/correction approaches are listed in Table 2. Unless otherwise stated, all trends in this study were computed using least squares linear regressions, and the confidence intervals were computed with autocorrelation adjustment (Wigley et al. 2006). In

general, the absolute values of the temperature anomaly trends obtained by the "SNO + constant bias" correction are larger than the other two approaches. The maximum relative difference between different approaches is around 17%–27%, depending on the channels.

Figure 2a shows the anomaly time series of T_2, T_3, and T_4 for individual satellites and their combined anomaly trends for the SNO + constant bias correction. The time series of individual satellites is represented by different colors. Because of zero biases and small σ in these different series, different satellites agree with each other on a point-by-point basis during overlapping observations. As an example, the volcanic eruption of Mt. Pinatubo in June 1991 caused a sudden jump in the lower-stratospheric temperature during 1992 and 1993, which is clearly indicated in the T_4 time series of both *NOAA-11* and *NOAA -12* with the same magnitude and phase. The 1998 El Niño event had the same signatures in both the T_2 and T_3 time series.

To understand the trend differences between the constant bias correction and the Christy correction, Fig. 2b shows the difference time series between the two corrections for T_4. As Fig. 2b shows, the large differences occur mainly after 1999. The reason for these differences is the varying treatment of the warm target temperature. In the constant bias correction, correcting the intersatellite biases does not change the variability and trend of the *NOAA-14* time series since only a constant is added to the unadjusted time series. For the Christy correction, however, a term $a_{14}T_w'(N14)$ with a target factor $a_{14} = 0.015$ is added to the *NOAA-14* time series. Therefore, the major variation in the *NOAA-14* warm target temperature after 1999 causes the differences in temperature time series and trends between the constant bias correction and the Christy correction. At this point, we have no preference as to which trend value is more reliable as both approaches remove the intersatellite biases with small σ in $\langle \Delta T_{j,k} \rangle$ (Fig. 1). In any case, however, since the trend differences between these varying corrections are only about 17%–27%, an average of them, which is also shown in Table 2, provides a favorite trend estimate. To be more precise in the trend determination, data from *NOAA-15* and other Advanced Microwave Sounding
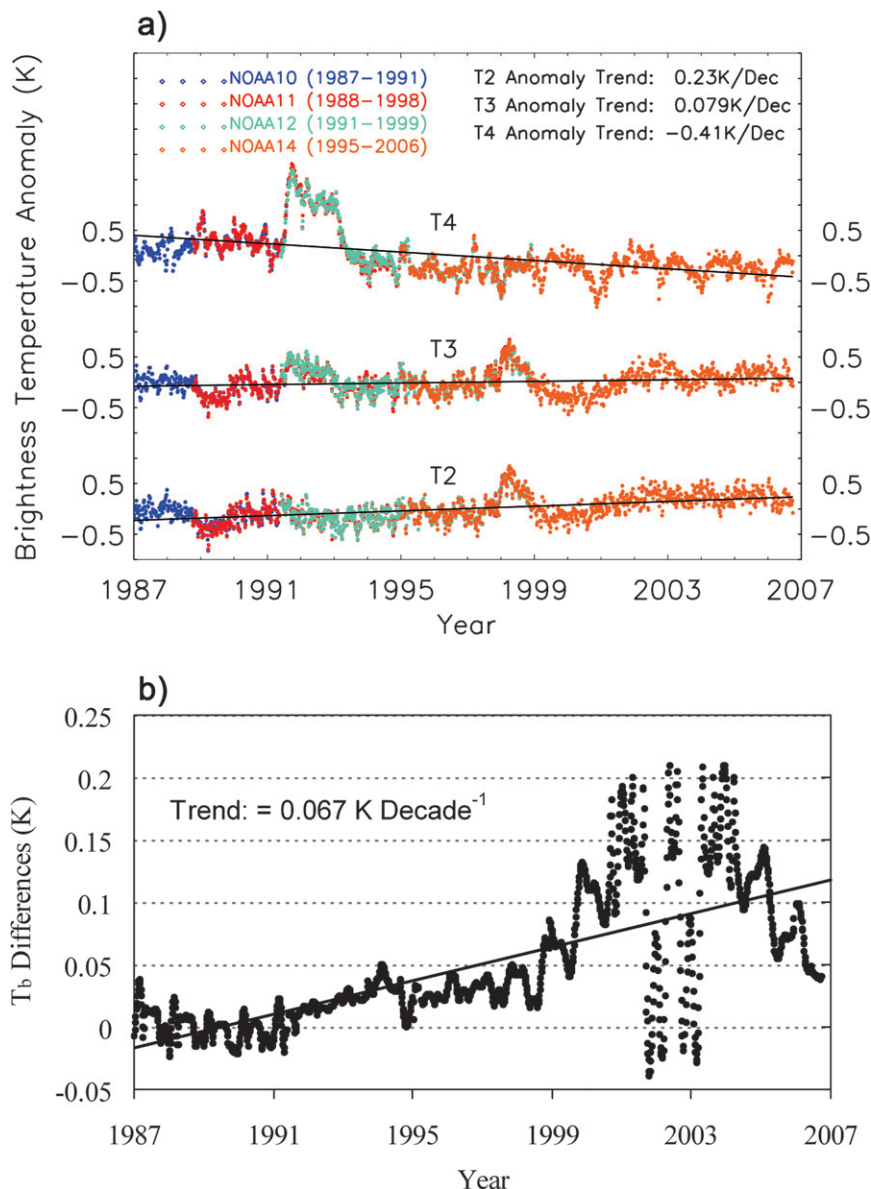
FIG. 2. (a) Anomaly time series and trends for the ocean mean T_2, T_3, and T_4 from January 1987 to September 2006 using the SNO calibration plus constant bias correction. (b) Time series difference for T_4 between the SNO + constant bias correction and SNO + Christy correction.

Unit (AMSU) satellites are required in the merging procedure to reduce the uncertainties after 1999.

However, the channel frequencies and footprint sizes of the MSU and AMSU observations are different, which adds further issues in merging them together. To deal with different channel frequencies, Goldberg and Fleming (1995) developed an algorithm that can generate an equivalent MSU channel-2 weighting function using a combination of different AMSU channels. Christy et al. (2003) included both the AMSU channel-5 and MSU channel-2 data in their temperature middle-troposphere

(TMT) time series using a constant bias correction to account for the frequency differences. The accuracies of these algorithms need to be tested in the SNO framework, which will be the focus of future studies.

4. Spatial pattern of the MSU temperature trend

a. Spatial pattern of intersatellite biases

To obtain the spatial pattern of the MSU trends and understand their accuracy, we must first examine the
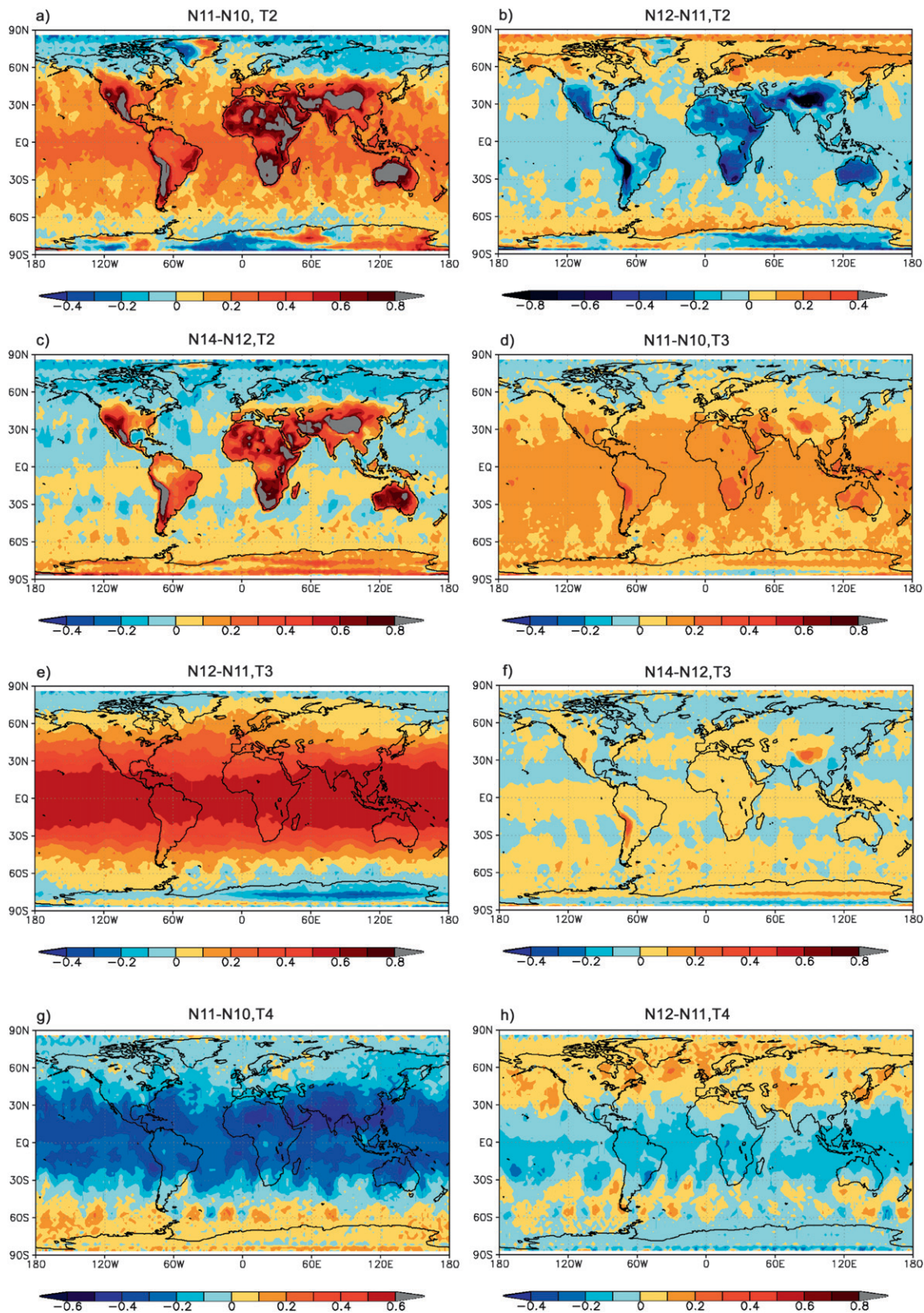
FIG. 3. Intersatellite bias patterns for different satellite overlaps and different channels after the SNO calibration. A total of seven limb-corrected footprints per scan line are used in the pentad dataset. Units are in K.
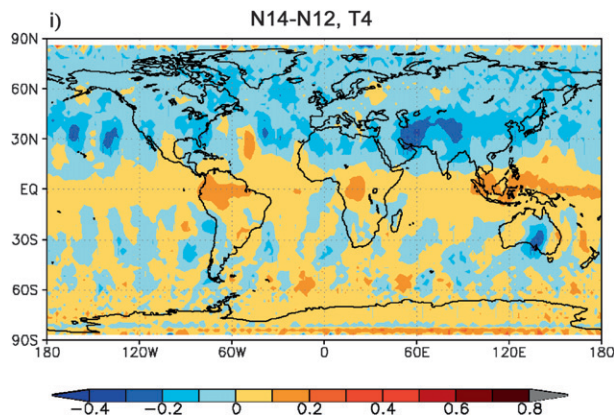
Fig. 3. (*Continued*)

spatial distribution of the intersatellite biases. Figure 3 shows the spatial pattern of the time-averaged T_b differences for *NOAA-11–NOAA-10*, *NOAA-12–NOAA-11*, and *NOAA-14–NOAA-12* during their overlapping observations. These figures include all T_2, T_3, and T_4 products after the SNO calibration and a total of seven near-nadir, limb-corrected footprints per scan line are included in the pentad dataset. The figure shows that the biases are within ±0.1 K over the ocean and most of the land areas for the *NOAA-14–NOAA-12* difference fields of T_3 and T_4 (Figs. 3f,i). Similar bias level is also found for the differences of *NOAA-12–NOAA-11* and *NOAA-14–NOAA-12* of T_2 over the oceans (Figs. 3b,c). These biases change signs for different latitudinal zones, resulting in near-zero global ocean mean differences for these satellite pairs owing to the cancellation effect (Fig. 1). This shows the SNO calibration works quite well for these overlaps.

The *NOAA-11–NOAA-10* difference of T_3 (Fig. 3d) and the *NOAA-12–NOAA-11* difference of T_4 (Fig. 3h) show medium biases (±0.2 K) over the tropics. However, relatively larger differences (about 0.3 K) near the peaks of the Andes and Himalaya mountains are found for all overlaps for T_3 (Figs. 3d–f). These differences occur because the surface elevation at these geographic locations is so high that the diurnal drift effect has a larger contribution to the channel 3 observations. For land areas with lower elevations, the diurnal drift effect is negligible for channels 3 and 4 as the intersatellite biases over these areas are the same as over the oceans. In any situation, however, the diurnal drift effect for channel 2 is important over land because bias differences between land and oceans are more apparent (~1 K over land but 0.2 K over oceans, Figs. 3a–c).

The *NOAA-11–NOAA-10* difference of T_2 and T_4 (Figs. 3a,g) and the *NOAA-12–NOAA-11* difference for T_3 (Fig. 3e) show larger latitudinal dependency, with smaller magnitude over the polar region and larger values over the tropics. This latitudinal dependency occurs partly because a single calibration coefficient for the nonlinear term cannot completely remove the warm target contamination (e.g., Fig. A1). Walker et al. (2004) show that the nonlinear response of a microwave detector could be different from the quadratic. It is very likely that more terms and coefficients in Eq. (1) are required for more accurate calibration and to more efficiently remove the warm target contamination when the quadratic approximation does not perform well.

Another explanation of this dependency involves the sampling errors. To demonstrate this, Fig. 4 shows the relationship between the intersatellite biases and the total numbers of the near-nadir, limb-corrected footprints per scan line used in the pentad datasets. Figure 4a shows the global ocean-averaged biases for all overlaps and all channels, and Fig. 4b is an ocean-only, zonal mean T_2 bias for *NOAA-11–NOAA-10*. Figure 4a (and also Fig. 3) show that the best result from the SNO calibration occurs at the *NOAA-14–NOAA-12* overlap, where the intersatellite bias is nearly exactly zero (less than 0.01 K) for all three channels and for all sampling numbers. The biases for *NOAA-11–NOAA-10* are between 0.1 and 0.2 K for different channels and pixel numbers. The largest bias occurs for *NOAA-12–NOAA-11* of channel 3 (0.4 K), although they are small (< 0.1 K) for channels 2 and 4 for this overlap.

Despite different values, a commonality in all these biases is that they are getting closer to zero, or at least remain the same (e.g., *NOAA-11–NOAA-10* of T_4) when the total number of footprints increases (except for *NOAA-12–NOAA-11* of T_2 at 11 footprints). Increasing the total number of the limb-corrected pixels is equivalent to increasing the samples in each grid cell. An immediate impact of this increase is that the larger orbital gaps in each pentad with fewer pixels (e.g., Fig. 5a for three pixels per scan line) have been greatly reduced with more pixel numbers (e.g., Fig. 5b for seven pixels per scan line). Because of the sampling increase from a total of one to nine footprints per scan line, we see a bias reduction of nearly 0.1 K for T_2 (*NOAA-11–NOAA-10*), T_2 (*NOAA-12–NOAA-11*), and T_3 (*NOAA-12–NOAA-11*). These bias reductions also suggest that the limb corrections work fairly well in correcting the angle effects.

b. Spatial pattern of the MSU trend from 1987 to 2006

Similar to the ocean means, the intersatellite biases at each grid cell must be removed to obtain the spatial pattern of the MSU trends. We use a procedure exactly the same as the ocean means to remove these biases—the
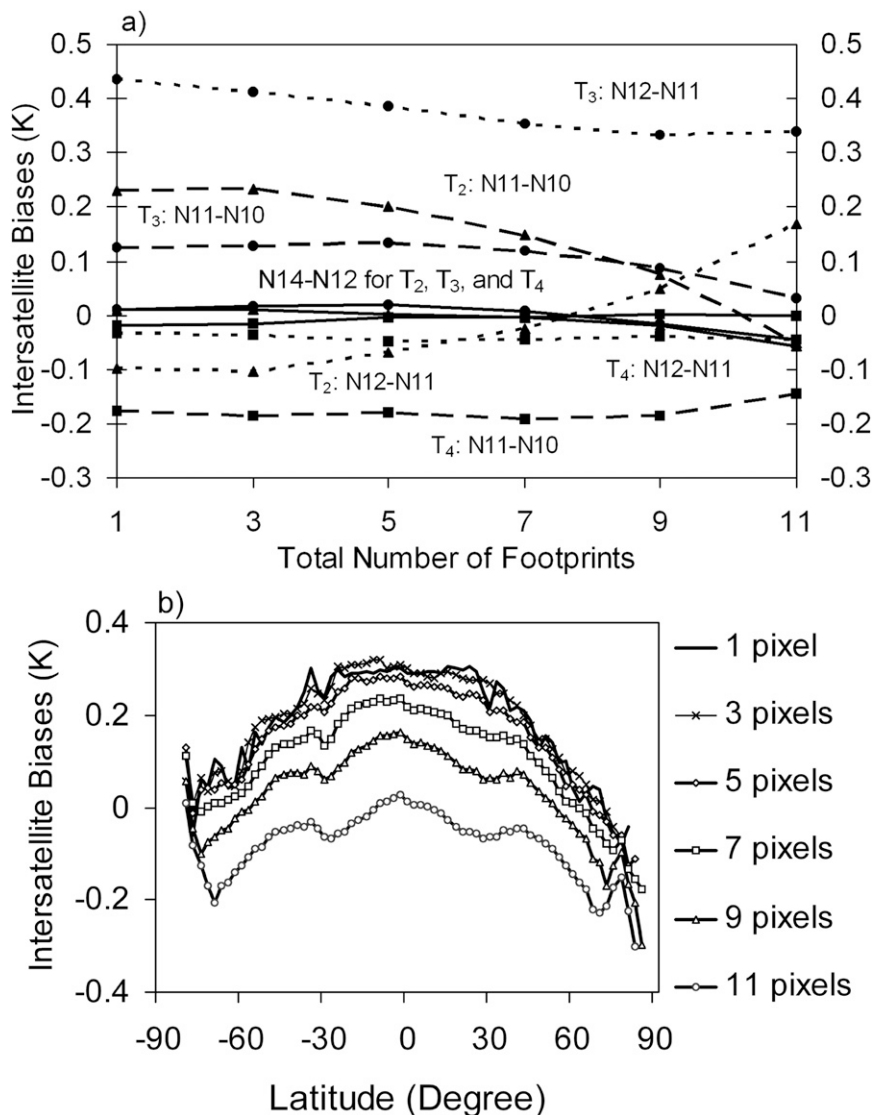
FIG. 4. Intersatellite biases vs the total number of footprints per scan line used in the pentad time series. (a) Global ocean mean biases for all overlaps and all three channels: T_2 (triangle), T_3 (dots), and T_4 (squares), and *NOAA-11–NOAA-10* (dashed), *NOAA-12–NOAA-11* (dotted), and *NOAA-14–NOAA-12* (solid). (b) Ocean-only, zonal mean T_2 biases for *NOAA-11–NOAA-10*.

time series on each grid cell is treated the same way as the ocean-mean time series so that intersatellite biases are removed completely for every grid cell. For the constant bias correction, this means that the constant bias used in the corrections is different for each grid cell (Fig. 3) and, after the correction, the intersatellite biases are reduced to zero at every geographic location for all overlaps (except for the *NOAA-14–NOAA-11* overlap that is not directly used in the correction; however, the corrected *NOAA-14–NOAA-11* bias is so small that it has negligible effect on the trend determination). For the Christy and Grody corrections, the correction coefficients are solved for each grid cell and are dependent

on latitude/longitude locations. These geographic location-dependent coefficients ensure near-zero intersatellite biases for all grid cells (on the order of 0.01–0.001 K). This is different from the studies of Christy et al. (2000, 2003) and Mears et al. (2003) in which zonal mean or global ocean mean data were used to determine the correction coefficients. Larger residual biases may still exist for individual grid cells if a constant empirical coefficient is used for the globe or a zonal circle.

Figure 6 shows the trend patterns of the three MSU channels after using the constant bias correction. This is, again, for the time series with seven near-nadir footprints.
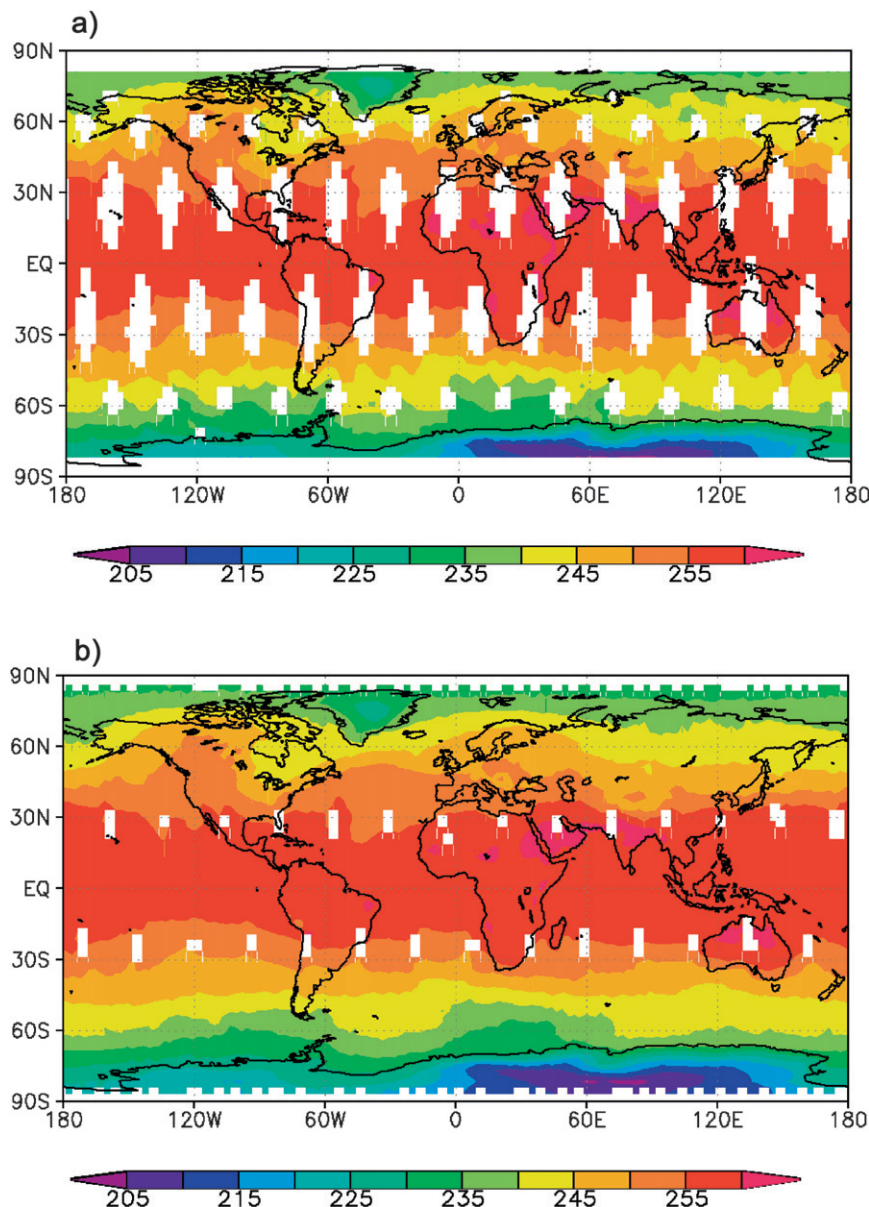
FIG. 5. Spatial pattern of the pentad T_2 for *NOAA-11* for the period of 1–5 Oct 1988: (a) three near-nadir, limb-corrected footprints per scan line are used in the pentad; (b) as in (a) but for seven near-nadir footprints per scan line. Units are in K.

For T_2, only trends over the ocean areas are shown because they are not accurate over land without a diurnal drift correction. The figure shows the global trends for T_3 and T_4 since a diurnal drift effect can be neglected globally (except over the peaks of the Andes and Himalaya mountains for T_3). The temperature trend patterns for the Christy correction are similar to the constant bias correction in general, but they look noisier owing to inhomogeneous correction coefficients.

Table 3 provides the global ocean mean trends computed from averaging the trend patterns. Note that the approach for computing this ocean mean trend (referred to as the "spatial trend pattern" approach) is different from the approach used in section 3 (results shown in Table 2) in which the global ocean mean time series for each satellite is obtained first and then the merging and trending is deduced from this ocean mean time series (referred to as the "ocean mean time series" approach). For the constant bias and Christy corrections, the ocean-mean trend values derived from the spatial trend pattern and the ocean-mean time series approaches agree well for all channels. This agreement
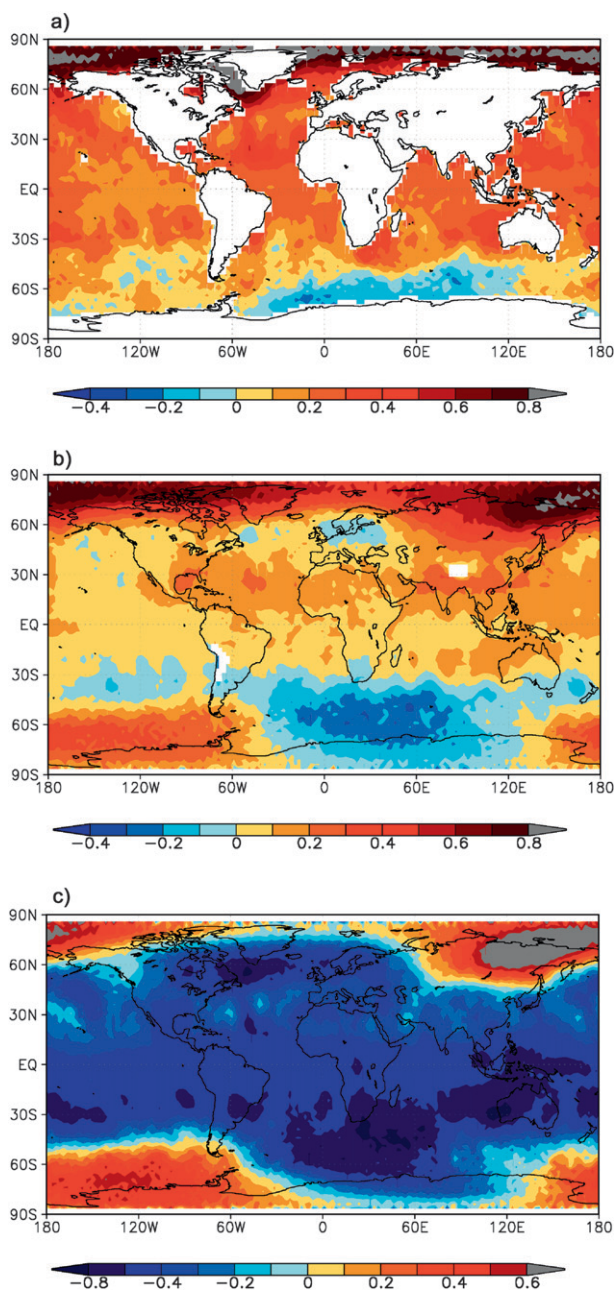
TABLE 3. Ocean-mean temperature anomaly trends (K decade^{-1}) from January 1987 to September 2006 obtained from averaging the spatial trend patterns. Errors are computed for a 95% confidence interval with autocorrelation adjustment.

	SNO + constant bias correction	SNO + Christy correction	% difference between the two methods	Averages of the two methods
T_2	0.214 ± 0.069	0.200 ± 0.067	7%	0.207 ± 0.068
T_3	0.075 ± 0.082	0.090 ± 0.080	18%	0.083 ± 0.081
T_4	-0.400 ± 0.272	-0.359 ± 0.262	10%	-0.379 ± 0.267

The Grody correction for the spatial trend pattern approach yields trends that are 0.15–0.20 K decade^{-1} warmer than its ocean-mean time series approach for all three channels. This difference occurs because the T_b value at a specific geographic location, especially over the high latitudes, is very different from the global mean. The fact that the correction term is nonlinearly dependent on the T_b makes the averaged correction coefficient a' in the spatial trend pattern approach different from a' in the ocean-mean time series approach. As these different a' values lead to larger trend differences, the Grody correction is not used in the following trend pattern discussion.

Figures 6a–c reveal some interesting features in the atmospheric temperature trends from 1987 to 2006. The trend values over the tropical and midlatitudes are generally close to the global means for all three channels. In particular, over the tropical region, the T_2 has a warming trend of about 0.2 to 0.3 K decade^{-1}. This warming trend gradually increases northward but decreases southward. The T_3 is warming at a rate less than the midtroposphere (T_2) over the tropics and midlatitudes for the same period ($\sim$0.1 K decade^{-1}), while the lower stratosphere (T_4) shows a large cooling trend ($\sim$ -0.5 K decade^{-1}) to compensate for the warming in the troposphere.

Over the Arctic Ocean, a significant warming occurs throughout the troposphere (for T_2 and T_3) at a rate of 0.6–0.8 K decade^{-1}. Over Antarctica, a cooling area across the southern Indian and Atlantic Oceans adjacent to Antarctica is found for all three channels. This cooling area and magnitude appears to get larger upward from the midtroposphere to the lower stratosphere. Over the southern Pacific Ocean, the T_2 trend is neutral, but a large warming trend (0.3–0.4 K decade^{-1}) is found in the upper troposphere and lower stratosphere. The T_3- or T_4-adjusted T_2 trend is negative over this region (see below).

Of particular interest is a relatively larger warming found for T_2 over the tip of the Antarctic Peninsula. This warming is isolated from the surrounding cooling area over the southern Atlantic Ocean. It is well known that in situ observations show that the Antarctic Peninsula

FIG. 6. Spatial patterns of the MSU temperature trends for the period from January 1987 to September 2006: (a) T_2, (b) T_3, and (c) T_4. Only ocean trends are shown for T_2 since diurnal drift errors over land have not yet been corrected for this channel. Units are in K per decade.

serves as an excellent mutual validation of the two approaches for the final trend patterns and their averages. The agreement occurs mainly because of the linear relationship involved in the constant bias and Christy corrections. Although linear, the two approaches cannot yield ocean-mean trend values exactly the same because of missing data issues.

is warming faster than the rest of the surrounding areas, resulting in significant ice sheet melting in this area (Solomon et al. 2007). It is rather encouraging to see that the MSU observations show similar warming trends for this particular small area. In addition, recent studies (e.g., Comiso et al. 2008) suggest that the sea ice melting trend over the Arctic has accelerated significantly from 1996 to 2007 in comparison to the 1978–96 period. This acceleration is coincident with the large warming trend in T_2 during the same period (Fig. 2), although T_2 does not directly represent the surface temperature. It would be interesting to see if there is a corresponding relationship between the large T_2 warming trend and the large sea ice melting trend over the Arctic area from 1996 to 2006. Comprehensive coupled ice–ocean–atmosphere models will be needed for such investigations.

In summary, over the tropics and midlatitudes, the atmospheric temperature trends reverse their sign from warming in the middle and upper troposphere to cooling in the lower stratosphere. Over the Arctic region, significant warming is found for the entire troposphere. The Antarctic shows warming in the west and cooling in the east, especially for T_3 and T_4.

c. Trend error analysis

To understand the uncertainties in the trend pattern, Figs. 7a,b show the spatial patterns of σ for the *NOAA-12–NOAA-11* differences for channels 2 and 3, respectively. Channel 4 has a similar σ pattern as for channel 2 with similar magnitude and, thus, is not shown. These patterns are representative of all overlaps since other overlaps for the same channel show almost the same pattern and magnitudes. In general, the σ for an individual grid cell is significantly larger than the global ocean means. These σ patterns exhibit good zonal uniformity, with smaller magnitude in the tropics (0.2–0.3 K) and increasing values poleward. Large σ ($\sim$0.8 K) are found over the 30° and 60° latitudinal belts for all three channels owing to gaps in these regions (Fig. 5).

Figures 8a,b further show the constant-bias-corrected time series for different satellites at two different grid cells (6.25°S, 6.25°W and 31.25°S, 6.25°W, respectively). The first site represents a tropical time series with smaller σ, while the second point represents sites with larger σ at the 30° and 60° latitudinal belts (Fig. 7). Comparing these plots with Fig. 2a, it is seen that, owing to large σ values, the time series at 31.25°S, 6.25°W have large scattering between satellites. For the tropical point 6.25°S, 6.25°W, however, different satellites agree fairly closely because of smaller σ. Therefore, from the merging point of view, the confidence in the tropical
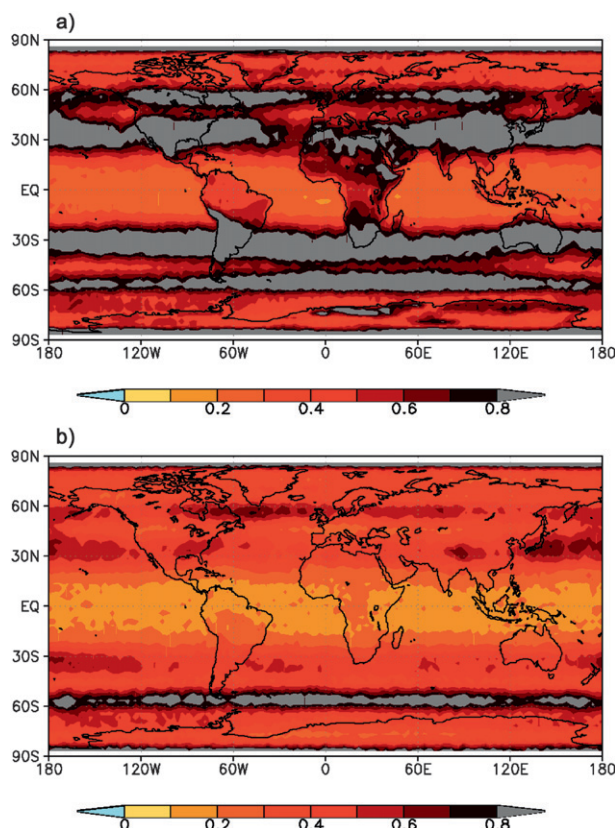

FIG. 7. Spatial patterns of σ (*NOAA-12–NOAA-11*) for (a) T_2 and (b) T_3. Units are in K.

trends should be higher than those at the 30° and 60° latitudinal belts.

Figure 9 shows the ocean-only, zonal mean temperature trends for all three channels and their associated 95% confidence intervals. The trends for both the SNO + constant bias correction and SNO + Christy correction are plotted. Consistent with ocean means, the two correction approaches result in similar spatial patterns for all three channels, except for an apparent deviation for T_3 over the tropics. This larger trend deviation in T_3 is associated with the large biases in $\langle \Delta T_{N11,N12} \rangle$ over the tropics (Fig. 3e). The error bar shows a general increase toward the poles as well as toward the equator from a minimum at the midlatitudes for all three channels. Over the polar region, the statistical errors are much larger than the trend itself for T_3 and T_4 ($\pm$0.6 K decade^{-1} for T_3 and $\pm$1 K decade^{-1} for T_4). This greater uncertainty is due to the larger interannual variability for high latitudes compared to the low latitudes. However, the T_2 trend is much larger than its error for most regions except over the Southern Ocean, indicating the robustness of the trends, especially over the Arctic region.
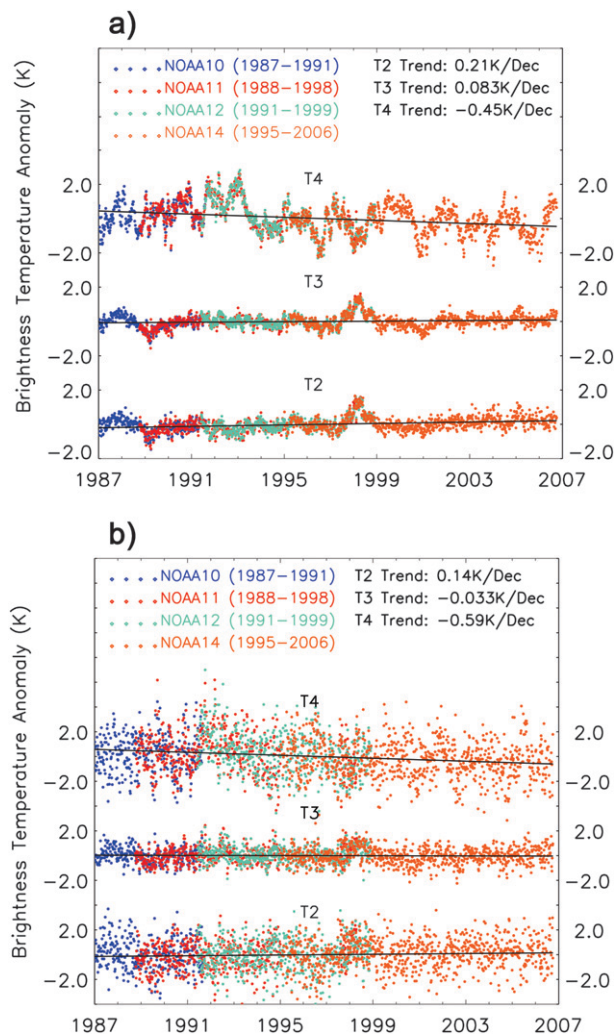
FIG. 8. Temperature anomaly time series and trends for SNO + constant bias correction at the geographic locations (a) 6.25°S, 6.25°W and (b) 31.25°S, 6.25°W.

Trend pattern differences from other studies can be seen by comparing the current study to the datasets from the University of Alabama in Huntsville (UAH) group (Christy et al. 2003) and the Remote Sensing System (RSS) group (Mears et al. 2003). We used UAH version 5.1 and RSS version 3.0 in our comparisons. These datasets use the prelaunch-calibrated radiances with zonal-mean gridded merging along with the MSU and AMSU observations. However, different methods in the diurnal drift corrections are used in these datasets. Large T_2 trend differences between the UAH dataset and this study are found over the tropics and subtropics. However, this study and the UAH data agree with each other fairly well over the Arctic for the T_2 trends and globally for the T_4 trends. The RSS T_2 trends are in between of UAH and this study, and its T_4
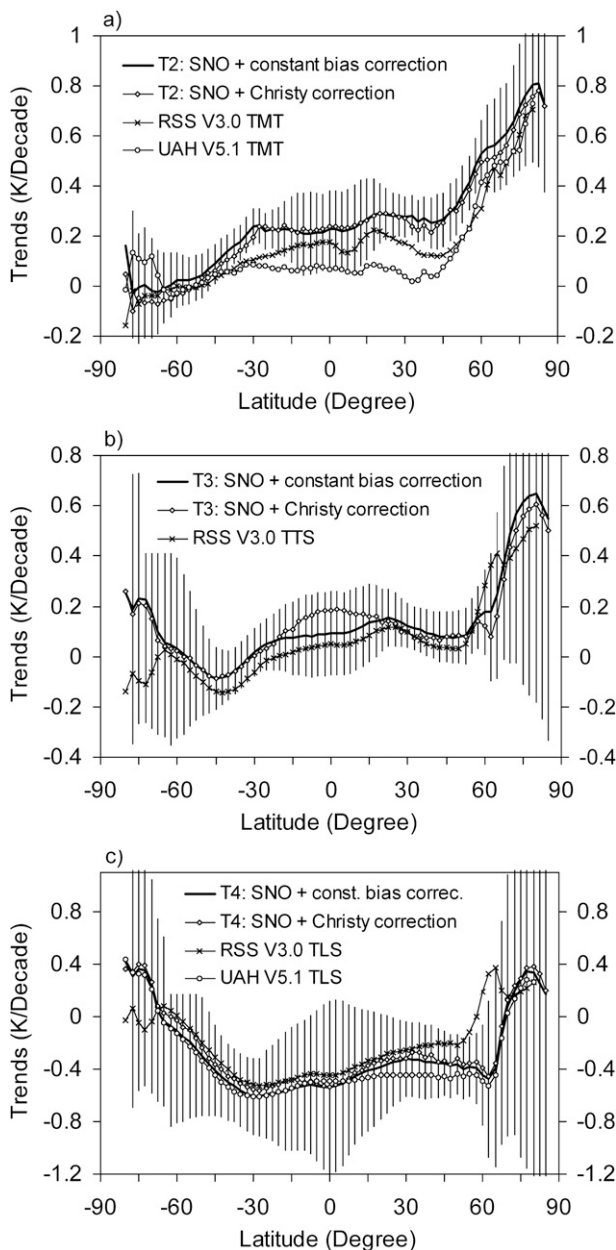

FIG. 9. Ocean-only, zonal mean trends and their error bars for 1987–2006 for (a) T_2, (b) T_3, and (c) T_4. Results from both the SNO + constant bias correction (bold line) and SNO + Christy correction (titled squares) are shown in the plot. Also shown are temperature trends for the same time period and spatial region from the RSS version 3.0 (crosses) and UAH version 5.1 (circles) datasets. Plots include temperature midtroposphere (TMT), temperature, tropopause and stratosphere (TTS), and temperature lower stratosphere (TLS). These are combined temperature products from the MSU and AMSU satellites resembling the MSU T_2, T_3, and T_4, respectively.

trend deviates noticeably from both the UAH and this study around 60°N and over the Antarctic. The T_3 trend patterns of RSS and this study agree well, but the RSS values are smaller over the tropics and subtropics.

To understand the trend consistencies between different channels, we consider the approach suggested by Fu et al. (2004). This method uses a combination of T_2 and T_4 to remove the lower-stratospheric cooling effect in T_2 and obtain more realistic midtropospheric temperature trends. The combination is linear so that the midtropospheric temperature trend, denoted as T_{24}, can be expressed as $T_{24} = \alpha_2 T_2 - \alpha_4 T_4$, where (α_2, α_4) are the regression coefficients. In the Fu et al. study, this pair of coefficients was equal to (1.156, 0.153) and (1.12, 0.11) for the global mean and tropical troposphere, respectively. The Fu global mean value resulted in a negative weighting function in T_{24} in the lower stratosphere, which may exaggerate the T_4 effect.

Recently, Spencer et al. (2006) modified these coefficients and suggested that the value (1.07, 0.07) would be more appropriate for the T_2 and T_4 combination. Johanson and Fu (2006) further argued that a coefficient pair of (1.141, 0.141) was robust in removing the global stratospheric effect since they resulted in small trend errors for different datasets. These coefficients were modified to be equal to (1.1, 0.1) over the tropics to account for the higher tropopause there (Fu and Johanson 2005). The weighting functions for T_2, T_3, T_4, and T_{24} with coefficients (1.07, 0.07) are shown in Fig. 10.

Since the T_3 trend is now available, we can also compute the midtropospheric temperature trend using a linear combination of T_2 and T_3, denoted as T_{23}. The combination coefficient for T_{23} obtained by Fu and Johanson (2005) is (1.69, 0.69). However, these coefficients also lead to a negative weighting function in the lower stratosphere (not shown). Here we have obtained another set of coefficients equal to (1.43, 0.43) using the retrieval algorithm of Goldberg and Fleming (1995). The T_{23} weighting function for this set of coefficients is also shown in Fig. 10. This function has positive values throughout the stratosphere. Although the T_{23} and T_{24} retrievals have slightly different contributions from the surface and upper troposphere, their weighting functions peak at nearly the same midtropospheric level. Therefore, both of them represent the midtropospheric temperature and their trend results can be used for mutual validation and to check the internal consistency of the individual channel trends.

Figures 11a,b show the midtropospheric temperature trend patterns for T_{23} with a coefficient of (1.43, 0.43) and T_{24} with a coefficient of (1.07, 0.07), respectively. Comparisons with the Fu coefficients are shown in Tables 4 and 5 . The two plots are very similar, in general, except that the T_{23} magnitude is a little larger than T_{24} in both the warming and cooling areas. In addition, the T_{23} and T_{24} trends exhibit some detailed differences from the T_2 pattern that dominates the overall pattern of the com-
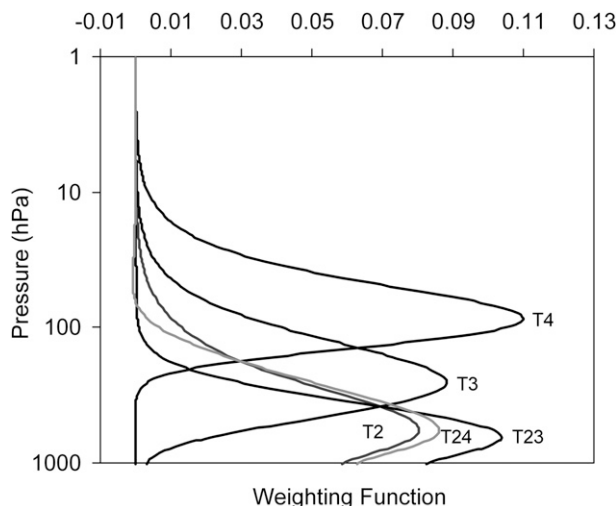

FIG. 10. Weighting functions for T_2, T_3, and T_4 and their combinations T_{23} and T_{24}. The combination coefficients are (1.43, 0.43) for T_{23} and (1.07, 0.07) for T_{24}, respectively.

binations. For instance, an enhanced warming of nearly 0.6–0.7 K decade^{-1} has been observed in both T_{23} and T_{24} trend patterns over the central northern Atlantic Ocean, but this warming is only 0.3–0.4 K decade^{-1} for T_2. The cooling area seen in T_2 across the southern Indian and Atlantic Oceans extends to nearly the entire Southern Ocean in T_{23} and T_{24}. We have also conducted point-by-point comparisons in a scatterplot and obtained good agreement between T_{23} and T_{24} trends (not shown). These similarities between T_{23} and T_{24} suggest that the channel trend patterns are internally consistent.

d. Trend comparisons from different studies

Tables 4 and 5 provide a summary of the global ocean and tropical ocean (20°S–20°N) mean temperature trends, respectively, during January 1987 to September 2006 for all three channels and their combinations for datasets from RSS, UAH, and the SNO + constant bias correction approach in this study. Sea surface temperature trends from Rayner et al. (2006) for the same period are also shown for an understanding of the vertical trend structure. For the global ocean T_2 trends, this study has the largest value (0.214 ± 0.069 K decade^{-1}) compared to the RSS (0.135 ± 0.113 K decade^{-1}) and UAH (0.080 ± 0.103 K decade^{-1}) datasets.

The T_3 trend of this study is also much larger than the RSS values for both global (0.075 ± 0.082 versus 0.022 ± 0.125 K decade^{-1}) and tropical (0.094 ± 0.159 versus 0.043 ± 0.188 K decade^{-1}) oceans. The global ocean T_4 trend of this study ($-0.400 ± 0.272$ K decade^{-1}) is between that of RSS ($-0.310 ± 0.364$ K decade^{-1}) and UAH ($-0.429 ± 0.397$ K decade^{-1}). The tropical ocean

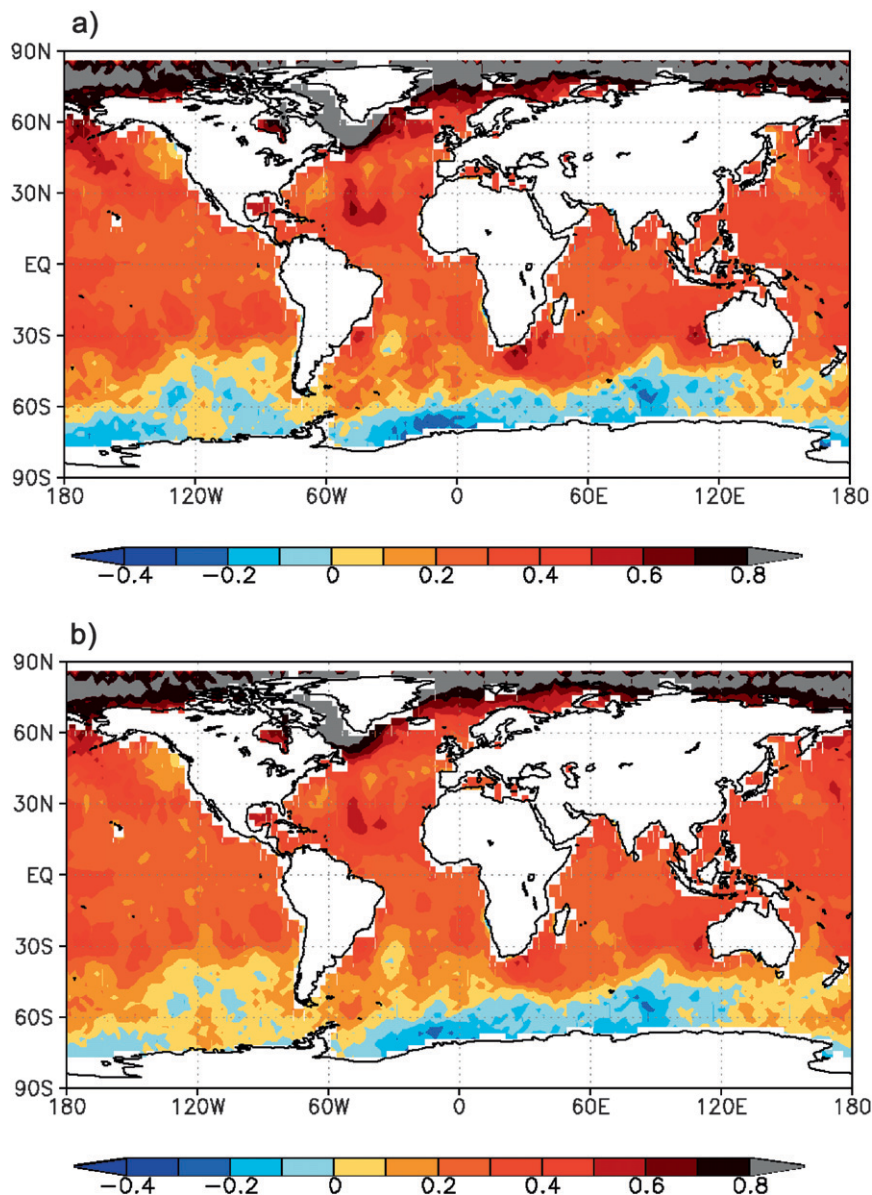FIG. 11. Trend patterns for (a) T_{23} and (b) T_{24}, during the time period from January 1987 to September 2006. The combination coefficients are (1.43, 0.43) for T_{23} and (1.07, 0.07) for T_{24}, respectively. Units are in K decade^{-1}.

T_2 trends of RSS (0.164 $\pm$ 0.229 K decade^{-1}) and this study (0.229 $\pm$ 0.165 K decade^{-1}) are larger than the surface trend (0.122 $\pm$ 0.219 K decade^{-1}). For both global and tropical oceans, the Fu and Johanson (2005) and Johanson and Fu (2006) coefficients result in larger T_{23} and T_{24} trends than the coefficients used in this study, but T_{23} agrees with T_{24} to within 0.02 K decade^{-1} for both sets of combination coefficients. This accuracy level holds for the trends of both the RSS and this study, showing internal consistency within these individual datasets.

The UAH T_2 trend is smaller than the surface trend for both global and tropical oceans, but its $T_{24\text{-Fu}}$ trend (0.126 $\pm$ 0.283 K decade^{-1}) is a little larger than the surface trend for the tropical oceans. In an Intergovernmental Panel on Climate Change (IPCC) project on model comparisons, Santer et al. (2005) found that the tropical atmospheric temperature trend was increasing vertically from the surface to about 300 mb for all 19 models used in the study, which was consistent with those predicted by the moist adiabatic lapse rate theory suggested by Stone and Carlson (1979). The T_{23} and T_{24}

TABLE 4. Global ocean-mean temperature anomaly trends of different atmospheric layers for the time period from January 1987 to September 2006. The combination coefficients for T_{23}, T_{24}, $T_{23\text{-Fu}}$, and $T_{24\text{-Fu}}$ are, respectively, (1.43, 0.43), (1.07, 0.07), (1.69, 0.69), and (1.141, 0.141). Errors are for a 95% confidence interval and units are in K per decade.

Dataset	SST	T_2	T_3	T_4	T_{23}	T_{24}	$T_{23\text{-Fu}}$	$T_{24\text{-Fu}}$
This study		0.214 ± 0.069	0.075 ± 0.082	−0.400 ± 0.272	0.274 ± 0.076	0.257 ± 0.078	0.310 ± 0.084	0.301 ± 0.089
RSS, version 3.0		0.135 ± 0.113	0.022 ± 0.125	−0.310 ± 0.364	0.183 ± 0.130	0.166 ± 0.129	0.212 ± 0.145	0.197 ± 0.149
UAH, version 5.1		0.080 ± 0.103		−0.429 ± 0.397		0.116 ± 0.117		0.152 ± 0.135
HADSST2*	0.177 ± 0.126							

* Met Office Hadley Centre's sea surface temperature dataset (Rayner et al. 2006).

trend results from this study and RSS dataset support these model results, although the magnitude of the amplification is different. For the global ocean means, the tropospheric amplification also occurs for temperature trends of this study, but is not obvious for the RSS and UAH datasets.

The trend patterns and their averages obtained in this study are quite stable when different total numbers of limb-corrected footprints are included in the pentad time series. Figure 12 shows how oceanic mean temperature trends vary with changes in the total footprint numbers per scan line. The plot contains trends for all three channels by the constant bias and Christy corrections. The maximum trend differences between different footprint numbers are within 0.02 K decade^{-1} (except for channel 2 at the 11 pixels) for all channels in the two different approaches, showing robust trend values and spatial patterns when more independent MSU pixel observations are included in the time series. One should also note that, except for channel 3 of the SNO + Christy correction, temperature trends for all of the different footprint numbers are close to that of the nadir observations (total footprint numbers per scan line equal to 1). This result shows that the limb corrections applied in this study do not affect the final trend results. Therefore, when noise is not a concern, one may just use the nadir observations to construct the time series and compute the trend.

5. Conclusions

We have intercalibrated the Microwave Sounding Units on the *NOAA-10*, *-11*, *-12*, and *-14* satellites using the simultaneous nadir overpass (SNO) method. In this method the radiance differences between pairs of satellite measurements are analyzed when both satellites are viewing the same area on the earth at the same time. Such SNO matchups occur in polar regions; nevertheless, the calibration coefficients obtained from the matchups are applied globally for the entire life cycle of each satellite. After the recalibration, intersatellite radiance biases at the SNO matchups are exactly zero. Mean biases in the global oceanic atmosphere of the gridded dataset generated from the recalibrated, limb-corrected radiances are generally O(0.05–0.1 K). This is an improvement of nearly an order of magnitude over use of the prelaunch calibration. Orbital-drift-related warm target contamination has been reduced to a minimum (nearly zero for channels 2 and 4) by the SNO calibration. This leads to stable intersatellite difference time series with an averaged standard deviation of 0.04 ~0.05 K for means of the global oceanic atmosphere.

Trend differences for two independent techniques for merging the data of overlapping satellite records—the SNO + constant bias and SNO + Christy methods—are minimal: only 0.015 K decade^{-1} for the midtroposphere (T_2) and tropopause layer (T_3) and 0.04 K decade^{-1} for

TABLE 5. As in Table 4, but for the tropical ocean (20°S–20°N). The combination coefficients for T_{23}, T_{24}, and $T_{23\text{-Fu}}$ are as in Table 4 but the coefficient for $T_{24\text{-Fu}}$ is replaced by (1.1, 0.1). Units are in K decade^{-1}.

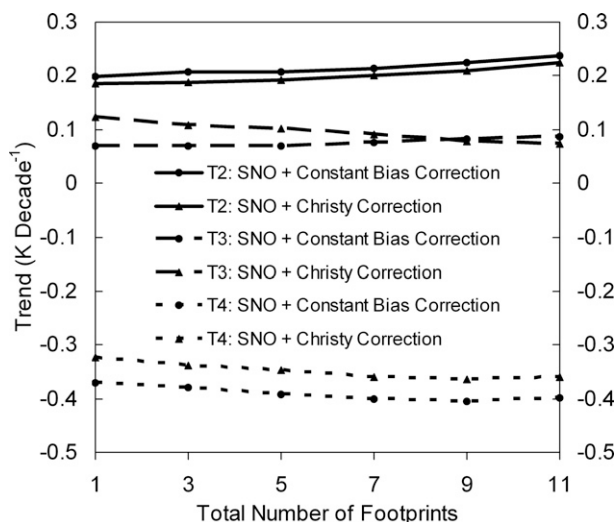| Dataset	SST	T_2	T_3	T_4	T_{23}	T_{24}	$T_{23\text{-Fu}}$	$T_{24\text{-Fu}}$
This study		0.229 ± 0.165	0.094 ± 0.159	−0.506 ± 0.514	0.286 ± 0.181	0.280 ± 0.191	0.322 ± 0.193	0.303 ± 0.202
RSS		0.164 ± 0.229	0.043 ± 0.188	−0.428 ± 0.459	0.216 ± 0.258	0.205 ± 0.269	0.247 ± 0.277	0.223 ± 0.286
UAH		0.069 ± 0.229		−0.502 ± 0.441		0.109 ± 0.267		0.126 ± 0.283
HadSST2 Rayner et al. (2006)	0.122 ± 0.219							

FIG. 12. Ocean mean temperature anomaly trends vs the total number of footprints per scan line used in the pentad time series.

the lower stratosphere (T_4). Mean trends of global oceanic atmosphere for T_2, T_3, and T_4 during 1987–2006 are respectively 0.207 ± 0.068, 0.083 ± 0.081, and -0.379 ± 0.267 K decade^{-1} for the average of the two merging techniques.

The derived trends are independent of the number of limb-corrected pixels used in the dataset. Two independent methods of removing the stratospheric contribution to T_2 (one using T_4 and one using T_3) yield similar midtropospheric temperature trends. These results indicate robust limb corrections and internal consistency in the calibration of the different channels.

By removing intersatellite biases for each grid cell, regional trends have been derived from the MSU observations. Large warming trends are found for most regions of the troposphere. The tropical midtroposphere (T_{24} or T_{23}) is found to be warming at a rate of 0.28 ± 0.19 to 0.32 ± 0.21 K decade^{-1} from 1987 to 2006. The Arctic troposphere is warming at 0.6 ± 0.2 to 0.8 ± 0.3 K decade^{-1} for the same period, which is two to three times faster than the global average. The upper troposphere is warming much faster than estimated by previous studies. Meanwhile, a cooling area is found throughout the atmosphere across the southern Indian and Atlantic Oceans adjacent to the Antarctic continent. However, because statistical uncertainty is high for the T_3 and T_4 trends over the polar region, one should expect the values to be highly variable for different statistical periods.

With the characteristics shown in this study, the MSU observations for the different NOAA satellites appear to be intercalibrated quite well, and they are expected to benefit future reanalysis in reducing spurious climate jumps and variability related to satellite transitions.

A Web site (online at http://www.orbit.nesdis.noaa.gov/smcd/emb/mscat/mscatmain.htm) has been created for the public to freely acquire the SNO-calibrated MSU dataset. The Web site contains both the intercalibrated radiance and gridded deep-layer temperature data from *NOAA-10* to *-14*. The last MSU satellite, *NOAA-14*, was decommissioned on 23 May 2007. Therefore, only the AMSU data are available after that. We plan to continue the time series by merging the AMSU and MSU observations using the SNO technique. In addition, the intercalibration work for satellites prior to *NOAA-10* is ongoing. Once these merges are completed, the updated datasets will be put on the designated Web site for the scientific community to use.

APPENDIX

A Sequential Procedure for Obtaining Calibration Coefficients from SNO

By applying the calibration, Eq. (1), to the SNO matchups between two satellites, represented by k and j, a radiance error between them is derived as

$$\Delta R = \Delta R_L - \Delta \delta R + \mu_k Z_k - \mu_j Z_j + E, \qquad (A1)$$

where $\Delta R_L = R_{L,k} - R_{L,j}$ and $\Delta \delta R = \delta R_k - \delta R_j$; E is a residual term related to the spatial and time differences between the satellites k and j and is ignored (Zou et al. 2006). All symbols in (A1) have the same meanings as Eq. (1) in the main text. In (A1), ΔR_L, Z_k, and Z_j are a function of the measurements, while $\Delta \delta R$, μ_k, and μ_j are unknown coefficients. The regression method is used to solve for these coefficients from the SNOs in which the summation of $(\Delta R)^2$ is minimized. However, because there is a high degree of colinearity between Z_k and Z_j for the SNOs, only $\Delta \delta R$ and the difference between μ_k and μ_j can be determined from regressions (Zou et al. 2006). Therefore, one of the satellites in the pair needs to be assumed as a reference satellite. As in previous

studies, *NOAA-10* is assumed to be the reference satellite for all channels, and its offset, δR_{N10}, is assumed to be zero. The sequential procedure as described in the following minimizes the warm target contamination, meaning choosing different reference satellites does not affect the final calibration and trend results.

For a given μ (and $\delta R = 0$) for *NOAA-10*, the calibration coefficients μ and δR for *NOAA-11* are obtained from regressions of the SNO matchups between *NOAA-10* and *-11* using Eq. (A1). Next, the coefficients for *NOAA-12* are obtained from the SNO matchups between *NOAA-11* and *-12*. Finally, *NOAA-14* coefficients are obtained from the SNO matchups between *NOAA-12* and *-14*. This is referred to as the sequential procedure. The problem is now reduced to the determination of the nonlinear coefficient μ_{N10} of the reference satellite. Once μ_{N10} is known, calibration coefficients for all other satellites are sequentially determined from their SNO matchups.

To obtain μ_{N10}, a series of sensitivity experiments are conducted in which the μ_{N10} changes from 0 to an arbitrary large value [12.5 (sr m^2 cm^{-1}) (mW)$^{-1}$ for all MSU channels]. For each given μ_{N10}, a set of calibration coefficients for all other satellites including *NOAA-11*, *-12*, and *-14* are obtained sequentially from regressions of their SNO matchups. For each set of calibration coefficients, a gridded pentad dataset and global ocean mean time series are generated following the procedure described in section 2 of this study with the same limb correction scheme. Following our previous study (Zou et al. 2006), we examine the coefficient of determination r^2, which is the square of the correlation coefficient between $\langle \Delta T_{j,k} \rangle$ and $\langle T_{w,j} \rangle$ or $\langle T_{w,k} \rangle$, where $\langle \Delta T_{j,k} \rangle$ represents the pentad, global ocean mean brightness temperature difference time series between the satellite pair j and k, and $\langle T_{w,j} \rangle$ and $\langle T_{w,k} \rangle$ are the warm target temperature time series for satellites j and k, respectively. The quantity r^2 measures how much of the variance in $\langle \Delta T_{j,k} \rangle$ can be explained by $\langle T_{w,j} \rangle$ or $\langle T_{w,k} \rangle$ in the overlapping observations. For each satellite, a special μ value exists where r^2 equals exactly zero (Zou et al. 2006). This relationship can be understood by examining the correlation behavior between the radiance (or brightness temperature T_b) and the warm target temperature T_w. From Eq. (1), their correlation is written as

$$\overline{R' T'_w} = \overline{R'_L T'_w} + \mu \, \overline{Z' T'_w}, \qquad (A2)$$

where the prime represents an anomaly and the overbar is an average over time. The T_b difference time series for overlapping satellites is the anomaly where the climate signals are excluded from the overlapping obser-
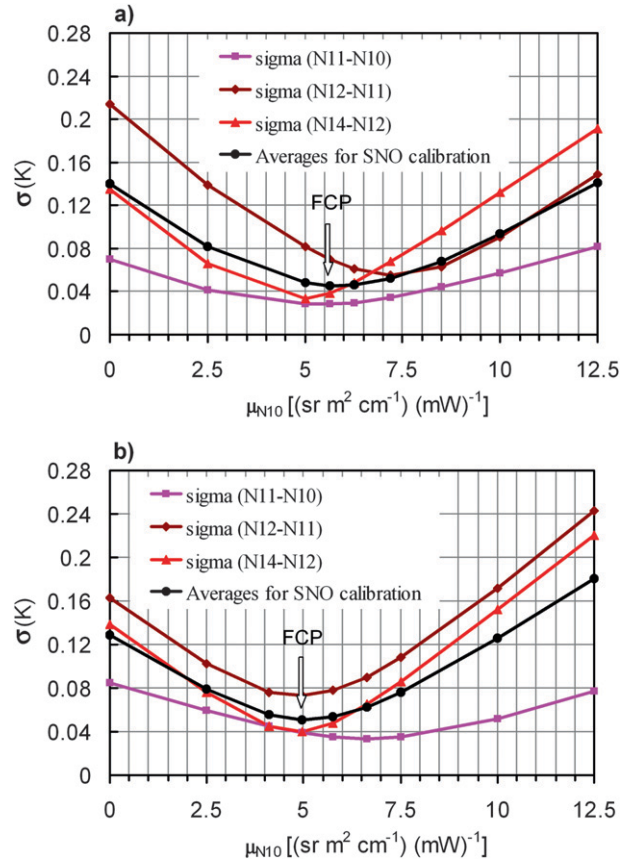

FIG. A1. Plot of $\sigma (\Delta T_{j,k})$ vs μ_{N10} in the sensitivity experiments for different satellite overlaps and their averages for MSU (a) channel 3 and (b) channel 4. The "Averages for SNO calibration" is a simple average over the three curves $\sigma(NOAA\text{-}11-NOAA\text{-}10)$, $\sigma(NOAA\text{-}12-NOAA\text{-}11)$, and $\sigma(NOAA\text{-}14-NOAA\text{-}12)$. The μ_{N10} values corresponding to the minimum in the "Averages for SNO calibration" are selected as the final calibration points (FCP).

vations so that only the instrument characteristics remain. It was found that the linear correlation term $\overline{R'_L T'_w}$ and the nonlinear correlation term $\overline{Z' T'_w}$ in Eq. (A2) are in opposite signs for each satellite (Zou et al. 2006). Thus, r^2 equals zero when

$$\mu = \mu_c = - \frac{\overline{R'_L T'_w}}{\overline{Z' T'_w}}. \qquad (A3)$$

In our previous study, the final μ_{N10} was chosen from the sensitivity experiments when the averaged r^2 over all satellite overlaps reaches a minimum. For MSU channel 2 for *NOAA-10*, *-11*, *-12*, and *-14*, this minimum is very close to zero at only 4% (Zou et al. 2006), suggesting nearly zero warm target contamination in the resulting time series. This result makes the merged dataset of high quality for climate trend study.

The principle of finding the minimum r^2 is also applied to channels 3 and 4 to obtain the final calibration point. In practice, however, we use the standard deviation (σ) of the $\langle \Delta T_{j,k} \rangle$ time series to replace r^2 in examining the contamination by the warm target temperature. The advantage of using σ is that this single variable includes the additive effect of the warm target temperature contamination by both satellites in the pair j and k. The reason for being able to use σ to replace r^2 is that the fluctuations or noise in $\langle \Delta T_{j,k} \rangle$ are mainly caused by satellite orbital drifts. Figures A1a,b show how the σ of $\langle \Delta T_{j,k} \rangle$ changes with μ_{N10} for the satellite pairs NOAA-10–NOAA-11, NOAA-11–NOAA-12, and NOAA-12–NOAA-14. The average over these σs is also shown in the figure to quantify the overall quality of the SNO calibration.

Based on the requirement of minimum warm target contamination in $\langle \Delta T_{j,k} \rangle$, the μ_{N10} value that results in the smallest averaged σ is selected as the final calibration point. From Fig. A1, these points are $\mu_{N10} = 5.63$ (sr m^2 cm^{-1}) (mW)$^{-1}$ for channel 3 and $\mu_{N10} = 4.95$ (sr m^2 cm^{-1}) (mW)$^{-1}$ for channel 4, respectively.

REFERENCES

Cao, C., M. Weinreb, and H. Xu, 2004: Predicting simultaneous nadir overpasses among polar-orbiting meteorological satellites for the intersatellite calibration of radiometers. *J. Atmos. Oceanic Technol.,* **21,** 537–542.

Christy, J. R., R. W. Spencer, and E. S. Lobel, 1998: Analysis of the merging procedure for the MSU daily temperature time series. *J. Climate,* **11,** 2016–2041.

——, ——, and W. D. Braswell, 2000: MSU tropospheric temperatures: Dataset construction and radiosonde comparisons. *J. Atmos. Oceanic Technol.,* **17,** 1153–1170.

——, ——, W. B. Norris, W. D. Braswell, and D. E. Parker, 2003: Error estimates of version 5.0 of MSU–AMSU bulk atmospheric temperature. *J. Atmos. Oceanic Technol.,* **20,** 613–629.

Comiso, J. C., C. L. Parkinson, R. Gersten, and L. Stock, 2008: Accelerated decline in the Arctic sea ice cover. *Geophys. Res. Lett.,* **35,** L01703, doi:10.1029/2007GL031972.

Fu, Q., and C. M. Johanson, 2004: Stratospheric influence on MSU-derived tropospheric temperature trends: A direct error analysis. *J. Climate,* **17,** 4636–4640.

——, and ——, 2005: Satellite-derived vertical dependence of tropical tropospheric temperature trends. *Geophys. Res. Lett.,* **32,** L10703, doi:10.1029/2004GL022266.

——, ——, S. G. Warren, and D. J. Seidel, 2004: Contribution of stratospheric cooling to satellite-inferred tropospheric trends. *Nature,* **429,** 55–58.

Goldberg, M. D., and H. E. Fleming, 1995: An algorithm to generate deep-layer temperature from microwave satellite observations for the purpose of monitoring climate change. *J. Climate,* **8,** 993–1004.

——, D. S. Crosby, and L. Zhou, 2001: The limb adjustment of AMSU-A observations: Methodology and validation. *J. Appl. Meteor.,* **40,** 70–83.

Grody, N. C., K. Y. Vinnikov, M. D. Goldberg, J. T. Sullivan, and J. D. Tarpley, 2004: Calibration of multisatellite observations for climate studies: Microwave Sounding Unit (MSU). *J. Geophys. Res.,* **109,** D24104, doi:10.1029/2004JD005079.

Hurrell, J. W., and K. E. Trenberth, 1997: Spurious trends in satellite MSU temperatures from merging different satellite records. *Nature,* **386,** 164–167.

——, and ——, 1998: Difficulties in obtaining reliable temperature trends: Reconciling the surface and satellite microwave sounding unit records. *J. Climate,* **11,** 945–967.

Johanson, C. M., and Q. Fu, 2006: Robustness of tropospheric temperature trends from MSU channels 2 and 4. *J. Climate,* **19,** 4234–4242.

Kidwell, K. B., Ed., 1998: NOAA Polar Orbiter Data user's guide. [Available online at http://www2.ncdc.noaa.gov/docs/podug/index.htm.]

Mears, C. A., and F. J. Wentz, 2005: The effect of diurnal correction on the satellite-derived lower tropospheric temperature. *Science,* **309,** 1548–1551.

——, M. C. Schabel, and F. J. Wentz, 2003: A reanalysis of the MSU channel 2 tropospheric temperature record. *J. Climate,* **16,** 3650–3664.

Mo, T., 1995: A study of the microwave sounding unit on the NOAA-12 satellite. *IEEE Trans. Geosci. Remote Sens.,* **33,** 1141–1152.

——, M. D. Goldberg, D. S. Crosby, and Z. Cheng, 2001: Recalibration of the NOAA microwave sounding unit. *J. Geophys. Res.,* **106,** 10 145–10 150.

Prabhakara, C., and R. Iacovazzi Jr., 1999: Comments on "Analysis of the merging procedure for the MSU daily temperature time series." *J. Climate,* **12,** 3331–3334.

——, ——, J.-M. Yoo, and G. Dalu, 2000: Global warming: Evidence from satellite observations. *Geophys. Res. Lett.,* **27,** 3517–3520.

Randall, R. M., and B. M. Herman, 2008: Using limited time period trends as a means to determine attribution of discrepancies in microwave sounding unit–derived tropospheric temperature time series. *J. Geophys. Res.,* **113,** D05105, doi:10.1029/2007JD008864.

Rayner, N. A., P. Brohan, D. E. Parker, C. K. Folland, J. J. Kennedy, M. Vanicek, T. Ansell, and S. F. B. Tett, 2006: Improved analyses of changes and uncertainties in marine temperature measured in situ since the mid-nineteenth century: The HadSST2 dataset. *J. Climate,* **19,** 446–469.

Santer, B. D., and Coauthors, 2005: Amplification of surface temperature trends and variability in the tropical atmosphere. *Science,* **309,** 1551–1556.

Smith, W. L., H. M. Woolf, P. G. Abel, C. M. Hayden, M. Chalfant, and N. Grody, 1974: NIMBUS-5 sounder data processing system. Part I: Measurement characteristics and data reduction procedures. NOAA Tech. Memo. NESS 57, 99 pp.

Solomon, S., D. Qin, M. Manning, M. Marquis, K. Averyt, M. M. B. Tignor, H. L. Miller Jr., and Z. Chen, Eds., 2007: *Climate Change 2007: The Physical Science Basis.* Cambridge University Press, 996 pp.

Spencer, R. W., and J. R. Christy, 1992a: Precision and radiosonde validation of satellite gridpoint temperature anomalies. Part I: MSU channel 2. *J. Climate,* **5,** 847–857.

——, and ——, 1992b: Precision and radiosonde validation of satellite gridpoint temperature anomalies. Part II: Tropospheric retrieval and trends during 1979–90. *J. Climate,* **5,** 858–866.

——, ——, W. D. Braswell, and W. B. Norris, 2006: Estimation of tropospheric temperature trends from MSU channels 2 and 4. *J. Atmos. Oceanic Technol.,* **23,** 417–423.

Stone, P. H., and J. H. Carlson, 1979: Atmospheric lapse rate regimes and their parameterization. *J. Atmos. Sci.,* **36,** 415–423.

Trenberth, K. E., and J. W. Hurrell, 1997: How accurate are satellite "thermometers"? *Nature,* **389,** 342–343.

Vinnikov, K. Y., and N. C. Grody, 2003: Global warming trend of mean tropospheric temperature observed by satellites. *Science,* **302,** 269–272.

——, ——, A. Robock, R. J. Stouffer, P. D. Jones, and M. D. Goldberg, 2006: Temperature trends at the surface and in the troposphere. *J. Geophys. Res.,* **111,** D03106, doi:10.1029/2005JD006392.

Walker, D. K., K. J. Coakley, and J. D. Splett, 2004: Nonlinear modeling of tunnel diode detectors. *Proc. IEEE 2004 Intl. Geoscience and Remote Sensing Symp. (IGARSS'04)*, Vol. 6, Anchorage, AK, IEEE, 3969–3972, doi:10.1109/IGARSS.2004.1369997.

Wentz, F. J., and M. Schabel, 1998: Effects of satellite orbital decay on MSU lower tropospheric temperature trends. *Nature,* **394,** 661–664.

Wigley, T. M. L., B. D. Santer, and J. R. Lanzante, 2006: Statistical issues regarding trends. *Temperature Trends in the Lower Atmosphere: Steps for Understanding and Reconciling Differences*, T. R. Karl et al., Eds., Climate Change Science Program and Subcommittee on Global Change Research, 129–139. [Available online at http://www.climatescience.gov/Library/sap/sap1-1/finalreport/sap1-1-final-all.pdf.]

Zou, C.-Z., M. D. Goldberg, Z. Cheng, N. C. Grody, J. T. Sullivan, C. Cao, and D. Tarpley, 2006: Recalibration of microwave sounding unit for climate studies using simultaneous nadir overpasses. *J. Geophys. Res.,* **111,** D19114, doi:10.1029/2005JD006798.